Computer simulation study of the nematic-vapour interface in the Gay-Berne model

Luis F. Rull[a] and José Manuel Romero-Enrique[a]

[a] Departamento de Física Atómica, Molecular y Nuclear, Area de Física Teórica, Universidad de Sevilla, Avenida de Reina Mercedes s/n, 41012 Sevilla, Spain

ARTICLE HISTORY
Compiled December 12, 2016

ABSTRACT
We present computer simulations of the vapour-nematic interface of the Gay-Berne model. We considered situations which correspond to either prolate or oblate molecules. We determine the anchoring of the nematic phase and correlate it with the intermolecular potential parameters. On the other hand, we evaluate the surface tension associated to this interface. We find a corresponding states law for the surface tension dependence on the temperature, valid for both prolate and oblate molecules.

KEYWORDS
Monte Carlo simulation; liquid crystal; Gay-Berne model; interfaces; anchoring; surface tension

1. Introduction

Liquid crystals are states of the matter which present long-ranged orientational order [1]. However, the presence of boundaries and/or external fields can frustrate this order, leading to the appearance of elastic deformations on the orientational order, or the emergence of topological defects. On the other hand, the bounding surface can also control the orientational ordering. In particular, the interfacial behaviour of liquid crystals shows peculiarities not observed in simple fluids, as the far-field orientational field can be determined by the presence of the interface. The nematic director orientation on both free nematic interfaces (i.e. in equilibrium with its vapour above the nematic-isotropic-vapour triple point) and isotropic-nematic interfaces can be either parallel, perpendicular or oblique with respect to the interface normal [2], leading to the so-called homeotropic, planar and tilted anchoring, respectively. The interfacial properties of the liquid crystals are essential for the development of display technologies [1, 3]. On the other hand, the nematic anchoring in the nematic-vapour interface, together with the elastic properties of the liquid crystal, are determinant to understand the conformation of nematic droplets [4–6], which have applications in molecular sensing [7–10] or electro-optic devices such as privacy windows [11–16]. From a microscopic point of view, the interfacial anchoring is well known to be determined by the intermolecular potential details. A generalized Van der Waals theory [17], based in the

CONTACT José M. Romero-Enrique. Email: enrome@us.es

expansion of the intermolecular potential in spherical harmonics, shows that the three types of anchoring can be observed with the appropriate choice of parameters [18, 19]. On the other hand, molecular simulations have also been used to understand how the interfacial anchoring is controlled by the interaction potential. For example, for hard body potentials it is shown that the anchoring is planar for prolate molecules and homeotropic for oblates [17]. When attractive interactions are included, its anisotropy also plays a role in the anchoring. For example, studies on lattice models show that different choices for the parameters which define the attractive part of the intermolecular potential can lead to either homeotropic or planar anchoring [20].

In this Paper we wish to consider the effect of both the repulsive and attractive parts of the intermolecular potential on the interfacial anchoring of nematic liquid crystals in equilibrium with their vapours, as well as the associated surface tension. For this purpose, we consider the Gay-Berne model [21], which has been extensively studied in the literature to model realistic liquid crystals. This model is characterized by two parameters κ and κ' which determine the anisotropy of the repulsive and attractive parts of the intermolecular potential, respectively, together with two adjustable constants μ and ν (see next Section). For example $(\kappa, \kappa', \mu, \nu) = (4.4, 20, 1, 1)$ has been used to parametrise the prolate p-terphenyl molecule [22, 23], and $(0.345, 0.2, 1, 2)$ for the triphenylene core discotic model [24]. Note that the parametrisation can change drastically when considering different mesogens, so it would be useful to identify which potential parameters are determinant for the liquid crystal interfacial properties. There are only a few computer simulation studies on interfaces of the Gay-Berne model, in comparison with other models, such as hard rod fluids [25]. Regarding the nematic-vapour interface, there are reports on prolate molecules with $\kappa = 2$ and 3 which show the possibility of having either homeotropic or planar anchoring [26–28]. These results could be explained by heuristic arguments which identify the ratio κ/κ' as the key factor to determine the nematic phase anchoring. On the other hand, in the nematic-isotropic interface, only planar anchoring has been reported [29, 30]. Finally, we are not aware of any study which considers the nematic-vapour coexistence for oblate molecules. Discotic liquid crystals stand for promising materials for technological applications [31] and they have been recently studied by using Gay-Berne [32, 33] and related models such as the Gay-Berne-Kihara model [34, 35].

The main goal of this paper is to study the nematic-vapour interface for a wide range of intermolecular potential parameters, corresponding to both prolate and oblate molecules, in order to identify the key elements of the intermolecular potential which determine the anchoring of the nematic with respect to its interface with a vapour phase. The paper is organized as follows. In Section 2 we will present the model and the simulation details. Our simulation results will be discussed in Section 3. We will end up with our conclusions in Section 4.

2. Simulation details

The Gay-Berne intermolecular potential between the molecules i and j can be written as [21]:

$$U_{ij}^{GB}(\mathbf{r}_{ij}, \mathbf{u}_i, \mathbf{u}_j) = 4\varepsilon(\hat{\mathbf{r}}_{ij}, \mathbf{u}_i, \mathbf{u}_j) \left[\rho_{ij}^{-12} - \rho_{ij}^{-6}\right] \tag{1}$$

where

$$\rho_{ij} = \frac{r_{ij} - \sigma(\hat{\mathbf{r}}_{ij}, \mathbf{u}_i, \mathbf{u}_j) + \sigma_0}{\sigma_0} \tag{2}$$

$\mathbf{u_i}$ is the unit vector along the symmetry axis of the molecule i, $r_{ij} = |\mathbf{r}_i - \mathbf{r}_j|$ is the distance along the intermolecular vector $\mathbf{r}_{ij}$ joining the centers of mass of the molecules and $\hat{\mathbf{r}}_{ij} = \mathbf{r}_{ij}/r_{ij}$. The anisotropic contact distance $\sigma(\hat{\mathbf{r}}_{ij}, \mathbf{u}_i, \mathbf{u}_j)$ and the depth of the interaction energy $\varepsilon(\hat{\mathbf{r}}_{ij}, \mathbf{u}_i, \mathbf{u}_j)$ depend on the orientational unit vector, the length to breath ratio ($\kappa = \sigma_{ee}/\sigma_{ss}$) and the energy depth anisotropy ($\kappa' = \epsilon_{ss}/\epsilon_{ee}$), which are defined as the ratio of the size and energy interactions parameters in the end-to-end (ee) and side-by-side (ss) configurations. Their expressions are given in terms of the lengthscale σ_0 and the energy unit ϵ_0 as:

$$\frac{\sigma(\hat{\mathbf{r}}_{ij}, \mathbf{u}_i, \mathbf{u}_j)}{\sigma_0} = \left[1 - \frac{\chi}{2}\left(\frac{(\hat{\mathbf{r}}_{ij}\cdot\mathbf{u}_i + \hat{\mathbf{r}}_{ij}\cdot\mathbf{u}_j)^2}{1+\chi(\mathbf{u}_i\cdot\mathbf{u}_j)} + \frac{(\hat{\mathbf{r}}_{ij}\cdot\mathbf{u}_i - \hat{\mathbf{r}}_{ij}\cdot\mathbf{u}_j)^2}{1-\chi(\mathbf{u}_i\cdot\mathbf{u}_j)}\right)\right]^{-1/2} \tag{3}$$

$$\frac{\varepsilon(\hat{\mathbf{r}}_{ij}, \mathbf{u}_i, \mathbf{u}_j)}{\epsilon_0} = [\epsilon_1(\mathbf{u}_i, \mathbf{u}_j)]^{\nu} \times [\epsilon_2(\hat{\mathbf{r}}_{ij}, \mathbf{u}_i, \mathbf{u}_j)]^{\mu} \tag{4}$$

where

$$\epsilon_1(\mathbf{u}_i, \mathbf{u}_j) = [1 - \chi^2(\mathbf{u}_i\cdot\mathbf{u}_j)^2]^{-1/2} \tag{5}$$

$$\epsilon_2(\hat{\mathbf{r}}_{ij}, \mathbf{u}_i, \mathbf{u}_j) = 1 - \frac{\chi'}{2}\left[\frac{(\hat{\mathbf{r}}_{ij}\cdot\mathbf{u}_i + \hat{\mathbf{r}}_{ij}\cdot\mathbf{u}_j)^2}{1+\chi'(\mathbf{u}_i\cdot\mathbf{u}_j)} + \frac{(\hat{\mathbf{r}}_{ij}\cdot\mathbf{u}_i - \hat{\mathbf{r}}_{ij}\cdot\mathbf{u}_j)^2}{1-\chi'(\mathbf{u}_i\cdot\mathbf{u}_j)}\right] \tag{6}$$

$\chi = (\kappa^2 - 1)/(\kappa^2 + 1)$ and $\chi' = [(\kappa')^{1/\mu} - 1]/[(\kappa')^{1/\mu} + 1]$. As in the original paper we choose $\mu = 2$ and $\nu = 1$ [21]. The parameter κ characterizes the molecular elongation along the main symmetry axis of the molecule. So, values of $\kappa > 1$ correspond to prolate molecules, and $\kappa < 1$ to oblates. On the other hand, if $\kappa = \kappa' = 1$, the Lennard-Jones potential is recovered.

In order to study the interfacial properties of the Gay-Berne model, we need to know its phase diagram. Unfortunately there are only a few computer simulation studies which consider the dependence of the phase diagram on the potential parameters. For $\kappa = 3$, the effect of κ' on the liquid-vapour coexistence was studied in Ref. [36] by Monte Carlo simulations in the Gibbs ensemble and using Gibbs-Duhem techniques. It was found evidences of nematic-vapour and isotropic liquid-vapour coexistence for $\kappa' = 1$ and $\kappa' = 1.25$. On the other hand, by fixing the value of $\kappa' = 5$, which was considered previously for $\kappa = 3$ [37], the authors considered the effect of increasing the molecular elongation from $\kappa = 3.2$ to $\kappa = 4$ [38], finding that for $\kappa = 4$ the vapour-isotropic critical point disappeared and only liquid isotropic-nematic coexistence is found. Regarding oblate molecules, most of the simulation studies focus on the nematic-columnar phase transition [24, 39–42]. However, no systematic study on the effect of κ and κ' has been performed for oblate molecules.

Due to the limited number of studies reported in the literature which consider the nematic-vapour coexistence in the Gay-Berne model, and the high computational time cost to obtain the full phase diagram, instead we followed the procedure used in Ref. [4] to generate configurations of the liquid (either nematic or isotropic) near coexistence with the corresponding vapour phase. In this technique, NpT Monte Carlo simulations

are performed at $p = 0$ from initial conditions such that the density is higher than the corresponding to the liquid in coexistence with the vapour at the same temperature. Due to the anisotropic character of the molecules, the volume changes were done by either changing isotropically the three box side lengths, keeping the box shape cubic, or by selecting randomly a side length to be changed. If the number of particles is large enough, the bulk results obtained in both procedures is the same. The simulations were organized in cycles, each one corresponding to N attempts to move and rotate a randomly chosen particle, and a volume change try, with N being the number of particles in the simulation box. During the simulation, the system density decreases until it reaches a value close to the coexistence value. If the densities of the coexisting phases are very different, large volume change fluctuations are rare enough to prevent the system to go to the vapour phase for short simulations. On the other hand, the values of the maximum attempted volume change in the simulation, ΔV, are small but such that the acceptance ration for the volume change in the simulation is always smaller than 35%.

Once we get a typical near-coexistence liquid configuration, whe put two empty boxes aside the original and perform NVT simulations in this new box using periodic boundary conditions on the enlarged simulation box. Now a simulation cycle corresponds to N attempts to move and rotate a randomly chosen particle. With this procedure, two (nematic or isotropic) liquid-vapour interfaces are formed perpendicular to the longest simulation side direction, which we set to be parallel to the z axis, provided that the temperature is below the critical point value. Now we increase or decrease the temperature until the nematic-isotropic-vapour or the vapour-nematic-smectic(columnar) triple point is reached. For these simulations, we use as initial configuration the output of the simulation from the previous temperature.

Instead the full Gay-Berne potential Eq. (1) we used a truncated and unshifted version which is zero when the distance between the molecular centers of mass is larger than some cutoff value r_c. No long-range corrections are considered. With respect to this value, there is some controversy regarding its choice. For example, in Ref. [43] a 30% increase in the surface tension of a Lennard-Jones fluid was reported when the cutoff changed from $r_c = 2.5\sigma$ to 3σ. In order to assess the optimal value of r_c, we performed simulations for different values of r_c for the case reported in Ref. [27]. Our results are shown in Table 1, indicating that, for $\kappa = 3$, we do not find significative differences for r_c larger than $5\sigma_0$. So, we choose $r_c = (\kappa + 2.0)\sigma_0$ for prolate molecules, while for oblates we will consider a fixed value $r_c = 3\sigma_0$. Nevertheless, long-range corrections have been shown to be important for the evaluation of the surface tensions in Lennard-Jones-based systems [44–46].

During the NpT simulation, we monitor bulk quantities like density $\rho_b = N/\langle V \rangle$, with N and V being the number of particles and the simulation box volume, respectively; the nematic order parameter S, defined as the largest eigenvalue of the nematic order tensor

$$Q = \left\langle \frac{1}{N} \sum_{i=1}^{N} \frac{3\mathbf{u}_i \otimes \mathbf{u}_i - I}{2} \right\rangle \tag{7}$$

with the associated eigenvector is the nematic director; or the average potential energy $\langle \sum_{i<j} U_{ij}^{GB} \rangle$. In addition, during the NVT simulations we evaluate the density profile

as:

$$\rho(z) = \frac{1}{V_b} \left\langle \sum_{i=1}^{N} \Theta(z_i - z)\Theta(z + \Delta z - z_i) \right\rangle \tag{8}$$

where $V_b = L_x L_y \Delta z$ is the volume of a slice perpendicular to the z axis, and $\Theta(x)$ is the Heaviside step function. We choose $\Delta z = 0.15\sigma_0$. The orientational order profile is characterized by the orientational order profile:

$$\overline{P}_2(z) = \left\langle \frac{1}{2N_k} \sum_{i=1}^{N_k} (3u_{z,i}^2 - 1) \right\rangle \tag{9}$$

N_k is the number of particles on the slice k, and $u_{z,i}$ is the z-component of the i-particle orientation unit vector $\mathbf{u}_i$. If particles are perfectly aligned parallel to the interface (i.e. perfect planar anchoring), $\overline{P}_2 = -1/2$. On the other hand, if molecules are pefectly aligned along the normal to the interface (i.e. perfect homeotropic anchoring), $\overline{P}_2 = 1$.

Finally, the surface tension γ was evaluated by using two different methods. First, we evaluated it by using the virial route:

$$\gamma_{virial} = \frac{1}{2} \int_0^{L_z} dz (P_N(z) - P_T(z)) \tag{10}$$

where the 1/2 factor is due to the presence of two liquid-vapour interfaces, and $P_N(z)$ and $P_T(z)$ are the normal and tangential components of the pressure tensor profile evaluated along the z axis:

$$P_N(z) = \rho(z) k_B T - \frac{1}{2V_b} \left\langle \sum_{i,j}^{(k)} z_{ij} \frac{\partial U_{ij}}{\partial z_{ij}} \right\rangle \tag{11}$$

$$P_T(z) = \rho(z) k_B T - \frac{1}{2V_b} \left\langle \sum_{i,j}^{(k)} \frac{1}{2} \left(x_{ij} \frac{\partial U_{ij}}{\partial x_{ij}} + y_{ij} \frac{\partial U_{ij}}{\partial y_{ij}} \right) \right\rangle = \frac{P_x(z) + P_y(z)}{2} \tag{12}$$

where the superindex k refers to the pair of molecules i and j where at least one of them is on the k slice.

One of the main issues for the surface tension evaluation by computer simulation is the choice of the number of particles. For hard body simulations under similar conditions, McDonald *et al.* found unexpected differences between the P_x and P_y components of the pressure tensor [47]. In order to avoid these finite size we compared our results with those obtained by using the expanded ensemble technique [48]. This method allows an efficient calculation of the free energy difference between two interfacial states at the same temperature, number of particles and volume, but different interfacial area. During the simulation, we combine translational and orientational moves with changes of the interfacial area. As the simulations are performed keeping V constant, an interfacial area change ΔA corresponds to a rescaling of the center of mass positions of the particles. The acceptance probability of transition between two

states with different interfacial areas A and $A + \Delta A$ in the expanded ensemble is:

$$P_{ij} = \min\{1, \exp[-\beta(\Delta U_{ij} - \Delta W_{ij}]\} \tag{13}$$

where ΔU_{ij} is the change of potential energy and ΔW_{ij} is the difference between the weight factors associated to the states with different interfacial area. We use two possible states: the unchanged state 0, and a state where the interfacial area has changed by a value ΔA. This procedure allows to evaluate the free-energy change ΔF as $\Delta F = -k_B T \ln(p_1/p_0) + \Delta W$, with p_1 and p_0 being the probabilities to visit the states 0 y 1 during the simulations in the expanded ensemble simulation (for more details see Ref. [48]). Finally, the surface tension can be evaluated as

$$\gamma_{EE} = \frac{\Delta F}{\Delta A} \tag{14}$$

Table 2 shows the values of the surface tension using the expanded ensemble technique for $\kappa = 6$, which is the most sensible case to the finite-size effects. Three different options to change the interfacial area were used: by changing only the length along either the x or the y axis, or by changing both L_x and L_y simultaneously. The probability p_1 to find any of the two states is also reported. As it can be seen, $N = 4000$ is the better choice as the differences between the different estimates are within the statistical errors.

For the simulation, we use reduced units. So, the reduced values of density ρ, energy U, temperature T and surface tension γ are defined as

$$\rho^* = \rho\sigma_0^3 \qquad U^* = \frac{U}{\epsilon_0} \qquad T^* = \frac{k_B T}{\epsilon_0} \qquad \gamma^* = \frac{\gamma\sigma_0^2}{\epsilon_0} \tag{15}$$

3. Results and discussion

We have studied by computer simulations the nematic-vapour interface for different Gay-Berne models, which mimic either calamitic or oblate nematogens. Typical snapshots of our simulations are shown in Fig. 1. For prolate molecules, we have studied the values of $\kappa = 4$ and 6, and for oblate molecules we have considered $\kappa = 0.3$ and 0.5. Different values of κ' are analysed for each κ. For prolate molecules, we followed the strategy considered in Ref. [38]. For $\kappa = 4$ we started with $\kappa' = 1$, which corresponds to a situation where nematic-vapour coexistence was found for $\kappa = 3$, and we decreased the value of κ' searching for this coexistence. Table 3 shows the results obtained for prolate molecules. The value of ρ^*_{bulk} corresponds to the value obtained for the liquid phase in the NpT simulations, except for the cases where smectic phases appear, which were not observed in the $p = 0$ simulations. The values of ρ^*_{bulk} are almost identical to those obtained from the density profile in the NVT simulations well inside the liquid region. In addition, we report the type of phase (either nematic phase N or smectic phase Sm), as well as the overall nematic order parameter S. The range of temperatures where coexistence between the nematic and an isotropic phase is observed is limited, but it increases as the value of κ' decreases. In the NVT simulations we find smectics in equilibrium with a virtually empty vapour phase at low temperatures, where the typical smectic layering emerges from the interface. The smectic ordering can also been characterized by the evaluation of the parallel and

perpendicular correlation distribution functions inside the condensed phase layer, in a similar way as it is done in bulk. An analysis of the in-layer structure shows hexatic order, indicating that the smectic phase is of B-type. On the other hand, we do not find vapour-isotropic liquid coexistence, even for the smallest value of $\kappa' = 0.15$. This implies that there is no critical point. As a consequence, the nematic phase is in equilibrium with an isotropic fluid with a density with changes continuously from vapour-like to liquid-like values. Thus, as the temperature is increased, only a homogeneous isotropic fluid is observed in the NVT simulations, since the the system cannot develop interfacial configurations when the coexisting densities are below some threshold due to the total number of particles constraint. So, in an effective way there is an upper limit for the temperature to observe coexistence between the nematic and isotropic phase in our method.

Fig. 2 shows the density and $\overline{P}_2$ profiles for $\kappa = 4$, $\kappa' = 0.15$ and $T^* = 4.1$ and $T^* = 4.6$. None of these profiles show any structure on the interfaces, but there is monotonous crossover from the bulk isotropic to the bulk nematic values. Note that at the highest temperature the isotropic fluid density $\rho^* = 0.101$ is close to the corresponding to the nematic case $\rho^* = 0.187$. In both cases, the nematic phase shows a planar anchoring on the nematic-isotropic fluid interface, since $\overline{P}_2$ is negative in the nematic phase. For prolate particles, we only observe planar anchoring for all the cases we studied (see Fig. 1a). In order to confirm this results, we performed additional simulations for selected conditions from initial conditions where the nematic showed a homeotropic alignment. Fig. 3 shows that the different nematic director components in the nematic region for $\kappa = 4$, $\kappa' = 1$ and $T^* = 0.80$ at nematic-vapour coexistence evolve to the planar configuration after approximately 10^6 cycles.

Oblate molecules (i.e. $\kappa < 1$) show a richer phenomenology. We choose two values of the molecular elongation parameter $\kappa = 0.3$ and 0.5. The results obtained from our computer simulations are summarised in Table 4. Now we find coexistence between the vapour and both nematic and isotropic liquid phases. Again the temperature range where nematic-vapour coexistence appears is limited, being slightly larger for $\kappa = 0.3$ than for $\kappa = 0.5$. At low temperatures, columnar phases appear in equilibrium with the vapour. On the other hand, as the temperature raises, a vapour-isotropic liquid-nematic triple point appears, and above it the vapour is in equilibrium with an isotropic liquid. As in the case of the smectic phase for prolate molecules, columnar phase can be identify from the analysis of the parallel and perpendicular pair correlation functions in the condensed phase layer.

Fig. 4 shows the density and $\overline{P}_2$ profiles for $\kappa = 0.3$ and $T^* = 2.20$ for $\kappa' = 0.2$ and $\kappa' = 0.3$. As for the prolate molecules case, these profiles smoothly crossover from vapour to nematic values across the nematic-vapour interface. We observe that for the smallest value of κ' planar anchoring is observed since $\overline{P}_2$ is negative in the nematic layer, while for the largest value the anchoring is homeotropic, i.e. $\overline{P}_2 \approx S$ in the nematic layer, with S being the nematic order parameter of the bulk phase. In fact, we observe that the anchoring is planar if $\kappa > \kappa'$, and homeotropic otherwise (see Table 4 and also Figs. 1b and 1c), independently of the temperature. This result is in agreement with the arguments reported in Ref. [28]. As in the case of the prolate molecules, we check this prediction by performing additional simulations starting from initial conditions with the "wrong" nematic anchoring. Fig. 5 shows the evolution of the components of the global nematic director for $\kappa = 0.3$, $\kappa' = 1$ and $T^* = 1.10$ at nematic-vapour coexistence. We see that, starting from a planar anchoring, the nematic starts to reorient until it reaches the true homeotropic anchoring. We note that the number of Monte Carlo cycles required is smaller than the corresponding

value for prolate molecules. This may be due to the role that the elastic deformations play in this orientation change.

However, under some conditions a nematic-like layer is formed in the isotropic liquid-vapour interface (see Fig. 1d). Fig. 5 shows the orientational order profiles for $\kappa = 0.5$ and $\kappa' = 0.3$, which corresponds to planar anchoring, and $\kappa = 0.5$ and $\kappa' = 1$, which corresponds to homeotropic anchoring, for a range of temperatures around the corresponding nematic-vapour-isotropic triple point. In both cases, the density profiles (not shown) do not differ from those discussed previously. However, in these cases we observe an enhancement of the orientational ordering on the interfaces: molecules align preferentially homeotropically on a layer at the interface, regardless the nematic anchoring away from the interface. This layer persists even above the nematic-vapour-isotropic triple point. For the case $\kappa = 0.5$ and $\kappa' = 0.3$, the nematic-like layer is of molecular width and it remains almost unchanged when crossing the triple-point temperature. On the other hand, the nematic-like layer becomes very wide for $\kappa = 0.5$ and $\kappa' = 1$ above the triple point, and it is preceded by a small order deplection layer. In fact, we observe a nematic-vapour interfacial configuration for $T^* = 0.51$, which is above the triple point from the NpT simulations. Fig. 7 shows the dependence on the number of particles of the orientational order profile of the nematic-vapour interfacial state for $\kappa = 0.5$, $\kappa' = 1$. and $T^* = 0.51$. We confirm that the isotropic phase is the equilibrium one at these conditions ($\overline{P}_2 \approx 0.1$ in the midpoint of the liquid layer), but its value decreases slowly with N. The explanation of this phenomenon lies on the wetting properties of the isotropic-vapour interface, since it is likely to be wet by the nematic phase at the triple point. However, we have not done a systematic study to confirm this point. In any case, the existence of wetting implies that the simulations must be done more carefully, as there is an additional finite-size dependence.

The values of the reduced nematic-vapour surface tensions reported in Tables 3 and 4 show a strong dependence on the Gay-Berne potential parameters (see also insets of Figs. 8 and 9). However, a scaling behaviour is observed with respect to the potential parameters by considering the arguments outlined in Ref. [28]. So, for homeotropic anchoring, the surface tension is expected to scale as $N^H \epsilon_{ee}/A$, where N^H is the number of particles on the interface of area A, an ϵ_{ee} is the scale of the intermolecular potential energy in the end-to-end configuration. Since $N^H/A \sim 1/\pi\sigma_{ss}^2$, where σ_{ss} is the closest distance between two particles in the side-to-side configuration, we find that $\gamma^H \sim \epsilon_{ee}/\sigma_{ss}^2$. For planar anchoring, similar arguments yield $\gamma^P \sim N^P \epsilon_{ss}/A$, and $N^P/A \sim 1/\pi\sigma_{ss}\sigma_{ee}$, so $\gamma^P \sim \epsilon_{ss}/\sigma_{ss}\sigma_{ee}$. Thus, $\gamma^H/\gamma^P \sim (\epsilon_{ee}\sigma_{ee})/(\epsilon_{ss}\sigma_{ss}) = \kappa/\kappa'$, which implies that homeotropic anchoring is favoured if $\kappa < \kappa'$, and planar anchoring otherwise. Our results confirm this prediction, since homeotropic anchoring is only observed for oblate molecules with $\kappa \leq \kappa'$ (see Table 4). These results suggest that we should use rescaled surface tensions $\gamma' = \gamma\sigma_{ss}^2/\epsilon_{ee} = 2\kappa\kappa'\gamma^*/(1+\kappa^2)$ for homeotropic anchoring, and $\gamma' = \gamma\sigma_{ss}\sigma_{ee}/\epsilon_{ss} = 2\kappa^2\gamma^*/(1+\kappa^2)$ for planar anchoring, to compare surface tensions for different values of κ and κ'. However, these arguments do not provide the scale for the temperature dependence of the nematic-isotropic surface tension. We argue that, when there is planar anchoring, the temperature scale for the surface tension change is given by the largest in-plane intermolecular attraction, which is $\epsilon_{ss} = \epsilon_0(\kappa^2+1)/(2\kappa\kappa')$ if $\kappa' < 1$, or $\epsilon_{ee} = \epsilon_0(\kappa^2+1)/(2\kappa)$ otherwise. For homeotropic anchoring, this scale is given by ϵ_{ss}. So, we should use a rescaled temperature $T' = 2\kappa\kappa' T^*/(1+\kappa^2)$ for cases with planar anchoring and $\kappa' < 1$, and $T' = 2\kappa T^*/(1+\kappa^2)$ otherwise. Fig. 8 represents the rescaled values of the nematic-isotropic surface tensions as a function of the rescaled temperature for planar anchoring and $\kappa' < 1$. Note that under the rescaling the original curves, depicted in the inset, collapse in a reasonable

way to a master curve. Note that these curves were obtained for both prolate and oblate molecules with very different molecular characteristics. On the other hand, Fig. 9 plots the rescaled nematic-isotropic surface tensions vs. the rescaled temperature for homeotropic anchoring. The collapse is less clear than for the planar anchoring case, but still we can see that trends are common except maybe for the case $\kappa = 0.3$ and $\kappa' = 1$, which has a larger slope than the other curves. In any case, by comparison with the original data shown in the inset, the rescaling has a reasonable performance.

4. Conclusions

In this paper we present Monte Carlo simulations of the nematic-vapour interface for the Gay-Berne model, corresponding to either prolate and oblate molecules. We characterize the density and orientational order parameter profiles, as well as the anchoring of the nematic phase with respect to the nematic-vapour interface. For $\kappa > \kappa'$ we find that the anchoring is planar, and homeotropic otherwise, regardless the particles being prolate or oblate. These findings are in agreement with heuristic arguments reported in the literature [28]. Under some circumstances, an enhanced orientational order is observed in the nematic-vapour interface. On the other hand, we studied the nematic-vapour surface tension as a function of the temperature. By a generalization of the arguments presented in Ref. [28], we find that by rescaling the surface tension and the temperature by factors which depend on both κ and κ', our simulation data satisfy approximately corresponding states laws for planar and homeotropic anchoring. This is a remarkable result, since they work for very different molecular geometries. We expect that these findings can be corroborated with other liquid crystal models.

Acknowledgments

We acknowledge financial support from the Portuguese Foundation for Science and Technology under Contract No. EXCL/FIS-NAN/0083/2012, the Spanish Ministerio de Economía y Competitividad through grant no. FIS2012-32455, and Junta de Andalucía through grant no. P09-FQM-4938, all co-funded by the EU FEDER.

References

[1] P.G. de Gennes and J. Prost, *The Physics of Liquid Crystals*, 2nd ed. (Oxford University Press, Oxford, 1995)
[2] T. J. Sluckin and A. Poniewierski in *Fluid Interfacial Phenomena*, edited by C. Croxton (Wiley, Nw York, 1986).
[3] M. Kleman and O. D. Lavrentovich, *Soft matter physics: and introduction*, 1st ed. (Springer-Verlag, New York, 2003).
[4] L. F. Rull, J. M. Romero-Enrique and A. Fernandez-Nieves, J. Chem. Phys. **137**, 034505 (2012).
[5] D. Vanzo, M. Ricci, R. Berardi and C. Zannoni, Soft Matter **8**, 11790 (2012).
[6] D. Vanzo, M. Ricci, R. Berardi and C. Zannoni, Soft Matter **12**, 1610 (2016).
[7] I. Lin, D. S. Miller, P. J. Bertics, *et al.*, Science **332**, 1297 (2011).
[8] V. Tomar, S. I. Hernandez, N. L. Abbott *et al.*, Soft Matter **8**, 8679 (2012).
[9] T. Bera, J. Deng and J. Fang, J. Phys. Chem. B **118**, 4970 (2014).

[10] M. Khan and S. Y. Park, Colloids Surf. B: Biointerfaces **127**, 241 (2015).
[11] R. L. Sutherland, V. P. Tondiglia, L. V. Natarajan, T. J. Bunning and W. W. Adams, Appl. Phys. Lett. **64**, 1074 (1994).
[12] T. J. Bunning, L. V. Natarajan, V. P. Tondiglia and R. L. Sutherland, Annu. Rev. Mater. Sci. **30**, 83 (2000).
[13] C. C. Bowley, P. A. Kossyrev, G. P. Crawford and S. Faris, Appl. Phys. Lett. **79**, 9 (2001).
[14] M. Jazbinsek, I. Drevensek, M. Zgonik, A. K. Fontecchio and G. P. Crawford, J. Appl. Phys. **90**, 3831 (2001).
[15] D. Rudhardt, A. Fernandez-Nieves, D. R. Link and D. A. Weitz, Appl. Phys. Lett. **82**, 2610 (2003).
[16] A. Fernandez-Nieves, D. R. Link and D. A. Weitz, Appl. Phys. Lett. **8**, 121911 (2006).
[17] M. M. Telo da Gama in *Observation and Simulation of Phase Transitions in Complex Fluis*, edited by M. Baus, L. F. Rull and J. P. Ryckaert (Kluwer Academic, Dordrecht, 1995).
[18] E. Martin del Rio, M. M. Telo da Gama, E. de Miguel and L. F. Rull, Phys. Rev., **E52**, 5028 (1995).
[19] E. Martin del Rio, M. M. Telo da Gama, E. de Miguel and L. F. Rull, Europhys. Letters **35**, 189-194 (1996).
[20] M. A. Bates, Phys. Rev., **E65**, 041706 (2002)
[21] J. G. Gay and B. J. Berne, J. Chem. Phys., **74**, 3316 (1981).
[22] G. Luckhurst and P. Simmonds, Mol. Phys. **80**,233 (1993).
[23] M. A. Bates and G. R. Luckhurst, J. Chem. Phys. 110, 7087 (1999).
[24] A. P. J. Emerson, G. R. Luckhurst and S. G. Whatling, Mol. Phys. **82**, 113 (1994).
[25] R. van Roij, M. Dijkstra and R. Evans, J. Chem. Phys. **113**, 7689 (2000).
[26] A. P. J. Emerson, S. Faetti and C. Zannoni, Chem. Phys. Lett. **271**, 241 (1997).
[27] E. Martin del Rio and E. de Miguel, Phys. Rev. E **55** 2916, (1997).
[28] S. J. Mills, C. M. Care, M. P. Neal and D. J. Cleaver, Phys. Rev. E **58**, 3284 (1998).
[29] M. Bates and C. Zannoni, Chem. Phys. Lett. **280**, 40 (1997).
[30] M. Bates, Chem. Phys. Lett. **288**, 209 (1998).
[31] R. J. Bushby and K. Kawata, Liq. Cryst. **38**, 1415 (2011).
[32] O. Cienega-Cacerez, J. A. Moreno-Razo, E. Diaz-Herrera and E. J. Sambriski, Soft Matter **10**, 3171 (2014).
[33] H. Sidky and J. K. Whitmer, Liq. Cryst. doi:10.1080/02678292.2016.1201869 (2016).
[34] B. Martínez-Haya and A. Cuetos, J. Chem. Phys. **131**, 074901 (2009).
[35] B. Martínez-Haya and A. Cuetos, Phys. Rev. E **81**, 020701(R) (2010).
[36] E. de Miguel, E. Martin del Rio, J. T. Brown and M. P. Allen, J. Chem. Phys., **105**, 4234 (1996).
[37] L. F. Rull, Physica, **A220**, 113 (1995).
[38] J. T. Brown, M. P. Allen, E. Martin del Rio and E. de Miguel, Phys. Rev., **E57**, 6685 (1998).
[39] M. A. Bates and G. R. Luckhurst, J. Chem. Phys. **104**, 6696 (1996).
[40] D. Caprioni, L. Bellier-Castella and J. P. Ryckaert, Phys. Rev. **E67**, 041703 (2003).
[41] L. Bellier-Castella, D. Caprioni and J. P. Ryckaert, J. Chem. Phys., **121**, 4847 (2004).
[42] D. Chakrabarti and D, J. Wales, Phys. Rev. E **77**, 051709 (1979).
[43] G. J. Gloor, G. Jackson, F. J. Blas and E. de Miguel, J. Chem. Phys., **123**, 134703 (1999).
[44] L. G. MacDowell and F. J. Blas, J. Chem. Phys. **131**, 074705 (2009).
[45] F. J. Blas, A. I. Montero-Ventas Bravo, J. Algaba, F. J. Martínez-Ruiz and L. G. MacDowell, J. Chem. Phys. **140**, 114705 (2014).
[46] F. J. Martínez-Ruiz and F. J. Blas, Mol. Phys. **113**, 1217 (2015).
[47] A. J. McDonald, M. P. Allen and F. Schmid. Phys. Rev. **E63**, 010701 (2000).
[48] E. de Miguel, J. Phys. Chem, **B112**, 4674 (2001)
[49] J. S. Rowlinson and B. Widom, *Molecular Theory of Capillarity*. Clarendon, Oxford, 1982).

Table 1. Influence of the Gay-Berne potential cut-off on the surface tension.

κ	κ'	T^*	r_c^*	γ
3	1	0.55	4	0.416
3	1	0.55	5	0.470
3	1	0.55	7	0.471
3	1	0.59	4	0.369
3	1	0.59	5	0.415
3	1	0.59	7	0.412

Table 2. Comparison between the surface tension values γ_{EE} obtained with different expanded ensemble techniques for $\kappa = 6$ and number of particles N. p_1 is the probability to visit the state 1 (see text for explanation).

Changed box side	N	p_1	γ_{EE}
L_x	1372	0.490 (22)	0.479 (17)
	4000	0.502 (21)	0.379 (12)
L_y	1372	0.514 (30)	0.395 (6)
	4000	0.507 (26)	0.374 (4)
L_x, L_x	1372	0.506 (24)	0.393 (9)
	4000	0.498 (17)	0.378 (7)

Table 3. Summary of the simulation results for prolate molecules (see text for explanation).

κ	κ'	T^*	ρ^*_{bulk}	$Phase$	S	ρ^*_{iso}	γ^*_{virial}	$Anchoring$
4	1	0.55	0.283 (2)	Sm	0.967 (2)			
4	1	0.60	0.261 (2)	N	0.954 (2)		0.529 (15)	P
4	1	0.65	0.251 (2)	N	0.937 (2)	0.001	0.445 (14)	P
4	1	0.70	0.241 (1)	N	0.923 (3)	0.005	0.417 (13)	P
4	1	0.75	0.233 (2)	N	0.900 (3)	0.008	0.314 (10)	P
4	1	0.80	0.221 (2)	N	0.871 (6)	0.015	0.209 (10)	P
4	0.5	0.80	0.297 (2)	Sm	0.981 (1)			
4	0.5	0.90	0.275 (2)	N	0.972 (2)		0.954 (30)	P
4	0.5	1.00	0.264 (2)	N	0.962 (2)		0.822 (20)	P
4	0.5	1.10	0.257 (2)	N	0.951 (2)	0.001	0.695 (18)	P
4	0.5	1.20	0.243 (2)	N	0.946 (2)	0.005	0.522 (17)	P
4	0.5	1.25	0.236 (2)	N	0.938 (2)	0.009	0.446 (15)	P
4	0.5	1.30	0.229 (2)	N	0.929 (3)	0.017 (1)	0.359 (12)	P
4	0.5	1.35	0.220 (2)	N	0.909 (5)	0.032 (2)	0.262 (7)	P
4	0.5	1.40	0.208 (4)	N	0.885 (6)	0.058 (2)	0.185 (9)	P
4	0.25	2.00	0.274 (9)	Sm	0.993 (10)			
4	0.25	2.10	0.249 (10)	N	0.961 (18)	0.006	0.921 (46)	P
4	0.25	2.20	0.242 (10)	N	0.957 (19)	0.011	0.853 (56)	P
4	0.25	2.30	0.235 (10)	N	0.952 (20)	0.023 (1)	0.654 (50)	P
4	0.25	2.40	0.227 (10)	N	0.940 (17)	0.035 (1)	0.506 (42)	P
4	0.25	2.50	0.215 (9)	N	0.931 (12)	0.055 (1)	0.387 (41)	P
4	0.25	2.60	0.203 (6)	N	0.903 (22)	0.072 (2)	0.303 (33)	P
4	0.25	2.70	0.201 (9)	N	0.875 (26)	0.086 (3)	0.243 (10)	P
4	0.25	2.80	0.183 (9)	N	0.761 (42)	0.095 (4)	0.197 (11)	P
4	0.25	2.90	0.174 (7)	N	0.703 (52)	0.104 (7)	0.147 (10)	P
4	0.15	3.40	0.246 (1)	Sm	0.96 (1)			
4	0.15	3.50	0.242 (1)	N	0.95 (1)	0.015	1.053 (80)	P
4	0.15	3.60	0.237 (1)	N	0.95 (1)	0.025	1.005 (78)	P
4	0.15	3.70	0.231 (1)	N	0.94 (1)	0.032	0.953 (69)	P
4	0.15	3.80	0.226 (1)	N	0.94 (2)	0.042 (1)	0.856 (62)	P
4	0.15	3.90	0.218 (1)	N	0.93 (2)	0.055 (1)	0.814 (65)	P
4	0.15	4.00	0.209 (1)	N	0.93 (2)	0.062 (1)	0.621 (53)	P
4	0.15	4.10	0.215 (1)	N	0.90 (3)	0.071 (2)	0.502 (25)	P
4	0.15	4.20	0.205 (2)	N	0.85 (4)	0.082 (2)	0.423 (22)	P
4	0.15	4.30	0.202 (4)	N	0.84 (5)	0.085 (4)	0.356 (15)	P
4	0.15	4.40	0.195 (3)	N	0.71 (6)	0.091 (5)	0.337 (16)	P
4	0.15	4.50	0.190 (2)	N	0.68 (7)	0.095 (5)	0.282 (15)	P
4	0.15	4.60	0.187 (5)	N	0.62 (7)	0.101 (5)	0.250 (18)	P
4	0.15	4.70	0.184 (5)	N	0.63 (8)	0.112 (7)	0.227 (18)	P
6	0.5	1.50	0.187 (3)	Sm	0.978 (3)			
6	0.5	1.60	0.178 (6)	N	0.963 (3)	0.005	0.678 (25)	P
6	0.5	1.70	0.172 (10)	N	0.905 (4)	0.012	0.502 (20)	P
6	0.5	1.75	0.168 (11)	N	0.873 (5)	0.017	0.445 (22)	P
6	0.5	1.80	0.161 (10)	N	0.817 (7)	0.021	0.385 (21)	P
6	0.5	1.85	0.157 (9)	N	0.797 (9)	0.025	0.361 (22)	P
6	0.5	1.90	0.152 (11)	N	0.781 (11)	0.031	0.324 (15)	P
6	0.5	2.00	0.148 (10)	N	0.774 (10)	0.042	0.220 (13)	P
6	0.5	2.10	0.137 (7)	N	0.743 (11)	0.049 (1)	0.169 (10)	P
6	0.5	2.20	0.128 (10)	N	0.735 (12)	0.055 (1)	0.152 (10)	P
6	0.5	2.30	0.126 (15)	N	0.740 (15)	0.061 (1)	0.127 (6)	P
6	0.25	3.30	0.185 (2)	Sm	0.984 (2)			
6	0.25	3.40	0.163 (4)	N	0.935 (3)	0.027	0.605 (29)	P
6	0.25	3.50	0.159 (5)	N	0.921 (3)	0.031	0.476 (26)	P
6	0.25	3.60	0.153 (4)	N	0.902 (4)	0.036	0.435 (27)	P
6	0.25	3.70	0.149 (2)	N	0.874 (7)	0.040	0.354 (41)	P
6	0.25	3.80	0.145 (3)	N	0.831 (6)	0.044	0.318 (19)	P
6	0.25	3.90	0.140 (4)	N	0.804 (7)	0.047 (1)	0.301 (20)	P

Table 4. Summary of the simulation results for oblate molecules (see text for explanation).

κ	κ'	T^*	ρ^*_{bulk}	$Phase$	S	ρ^*_{vapor}	γ^*_{virial}	$Anchoring$
0.3	0.4	1.20	3.41 (3)	C	0.92			
0.3	0.4	1.30	3.24 (2)	N	0.89		12.28 (12)	H
0.3	0.4	1.40	3.17 (2)	N	0.87		11.36 (11)	H
0.3	0.4	1.50	3.12 (1)	N	0.84		10.51 (10)	H
0.3	0.4	1.60	3.01 (1)	N	0.81		9.25 (9)	H
0.3	0.4	1.70	2.94 (1)	N	0.77		8.20 (9)	H
0.3	0.4	1.80	2.84 (1)	N	0.73	0.01	7.06 (8)	H
0.3	0.4	1.90	2.73 (1)	N	0.65	0.02	5.73 (6)	H
0.3	0.4	2.00	2.21 (1)	I		0.04	3.82 (6)	
0.3	0.3	1.40	3.38 (7)	C	0.95			
0.3	0.3	1.50	3.24 (3)	N	0.88		14.00 (2)	H
0.3	0.3	1.60	3.16 (3)	N	0.87		12.80 (2)	H
0.3	0.3	1.70	3.10 (4)	N	0.84		11.81 (2)	H
0.3	0.3	1.80	3.03 (4)	N	0.83		10.58 (1)	H
0.3	0.3	1.90	2.95 (4)	N	0.78		9.43 (1)	H
0.3	0.3	2.00	2.88 (5)	N	0.73	0.01	8.30 (2)	H
0.3	0.3	2.10	2.78 (6)	N	0.66	0.02	6.96 (1)	H
0.3	0.3	2.20	2.65 (7)	N	0.55	0.03	5.56 (1)	H
0.3	0.3	2.30	2.08 (8)	I		0.05	3.51 (1)	
0.3	0.2	2.10	3.14 (10)	C	0.93			
0.3	0.2	2.20	3.06 (10)	N	0.90		12.83 (16)	P
0.3	0.2	2.30	3.00 (15)	N	0.89		11.52 (15)	P
0.3	0.2	2.40	2.94 (14)	N	0.79	0.01	10.31 (15)	P
0.3	0.2	2.50	2.86 (10)	N	0.76	0.02	8.99 (13)	P
0.3	0.2	2.60	2.79 (10)	N	0.72	0.03	7.78 (13)	P
0.3	0.2	2.70	2.70 (9)	N	0.65	0.05	6.37 (10)	P
0.3	0.2	2.80	2.58 (9)	N	0.47	0.06	4.43 (9)	P
0.3	0.2	2.90	2.08 (10)	I		0.10	2.82 (13)	
0.5	1.0	0.30	2.12 (1)	C	0.85			
0.5	1.0	0.40	1.97 (2)	N	0.77		4.22 (8)	H
0.5	1.0	0.50	1.86 (2)	N	0.50		3.56 (8)	H
0.5	1.0	0.60	1.75 (2)	I		0.001	3.27 (9)	
0.5	0.7	0.30	2.12 (10)	C	0.83			
0.5	0.7	0.40	1.99 (9)	N	0.74		5.16 (9)	H
0.5	0.7	0.50	1.89 (6)	N	0.48		4.28 (6)	H
0.5	0.7	0.60	1.78 (13)	I	0.45		3.94 (5)	
0.5	0.6	0.30	2.15 (9)	C	0.85			
0.5	0.6	0.40	2.03 (5)	N	0.73		5.31 (9)	H
0.5	0.6	0.50	1.94 (9)	N	0.61		4.61 (7)	H
0.5	0.6	0.60	1.80 (7)	I			4.18 (6)	
0.5	0.5	0.40	2.16 (3)	C	0.84			
0.5	0.5	0.50	1.97 (4)	N	0.62		5.31 (9)	H
0.5	0.5	0.60	1.82 (6)	I			4.69 (8)	
0.5	0.4	0.50	2.04 (5)	C	0.87			
0.5	0.4	0.60	1.91 (7)	N	0.48		5.35 (8)	P
0.5	0.4	0.70	1.79 (6)	I			4.64 (8)	
0.5	0.3	0.70	1.95 (4)	C	0.80			
0.5	0.3	0.80	1.85 (5)	N	0.44		5.24 (7)	P
0.5	0.3	0.90	1.73 (3)	I			4.45 (7)	
0.5	0.2	1.00	2.04 (3)	C	0.873			
0.5	0.2	1.10	1.85 (11)	N	0.662		5.63 (7)	P
0.5	0.2	1.20	1.76 (12)	N	0.536		4.98 (7)	P
0.5	0.2	1.30	1.64 (15)	I			4.59 (4)	

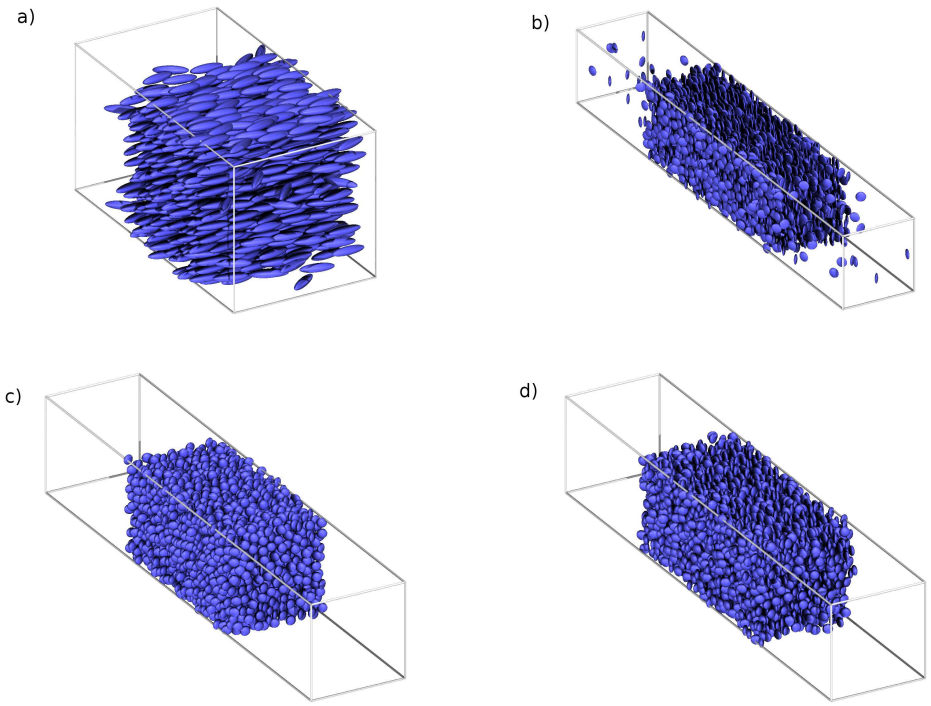

Figure 1. Snapshots of the interfacial simulations of the GB model with: (a) $\kappa = 4$, $\kappa' = 0.5$, $T^* = 1.20$ and $N = 1372$; (b) $\kappa = 0.3$, $\kappa' = 0.2$, $T^* = 2.50$ and $N = 4116$; (c) $\kappa = 0.5$, $\kappa' = 0.6$, $T^* = 0.40$ and $N = 4116$; and (d) $\kappa = 0.5$, $\kappa' = 1.0$, $T^* = 0.55$ and $N = 4116$.

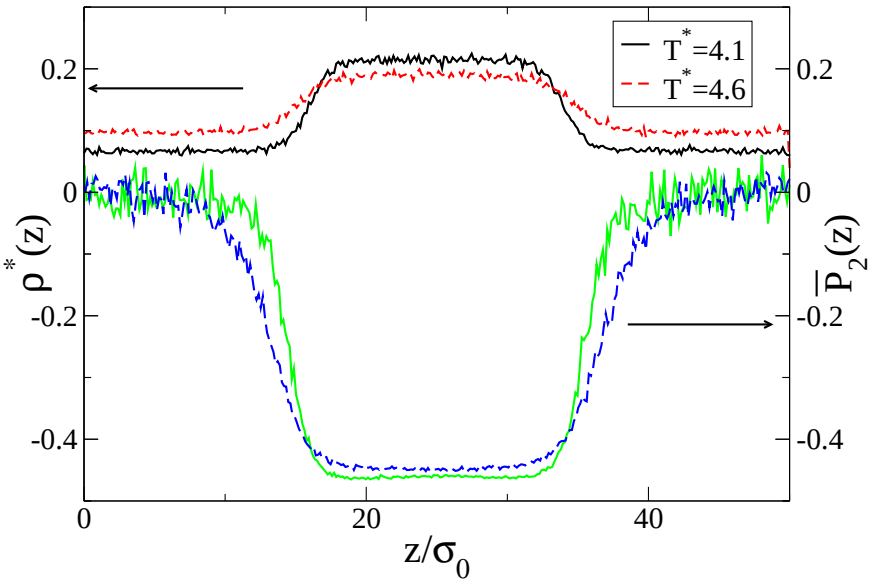

Figure 2. Density ρ^* (upper curves) and orientational order $\overline{P}_2(z)$ (lower curves) profiles for a Gay-Berne fluid with $\kappa = 4$ and $\kappa' = 0.15$, for $T^* = 4.1$ (continuous lines) and $T^* = 4.6$ (dashed lines).

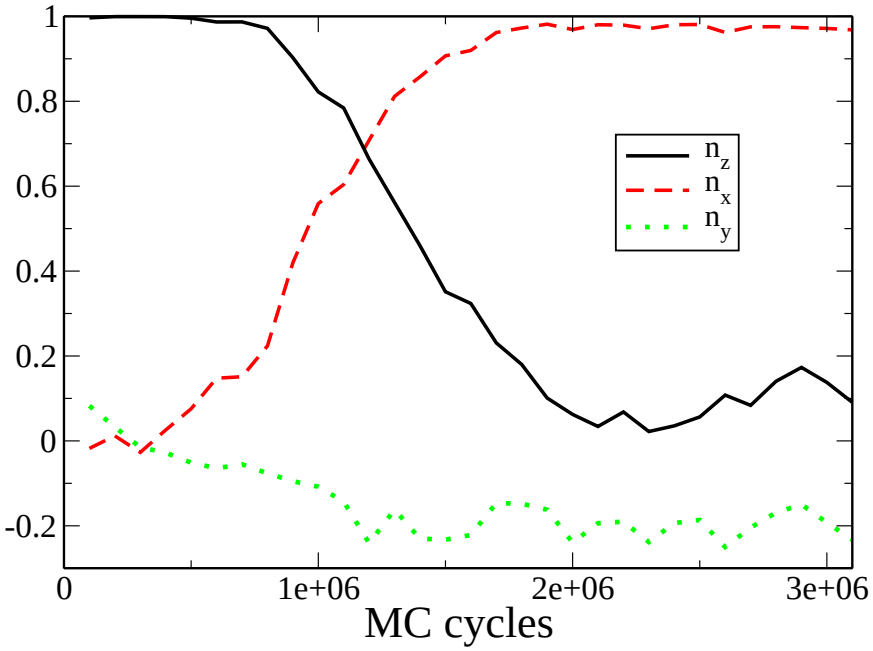

Figure 3. Evolution of the nematic director components for a Gay-Berne fluid with $\kappa = 4$ and $\kappa' = 1$ for $T^* = 0.8$ in presence of a nematic-vapour interface, starting at a homeotropic configuration.

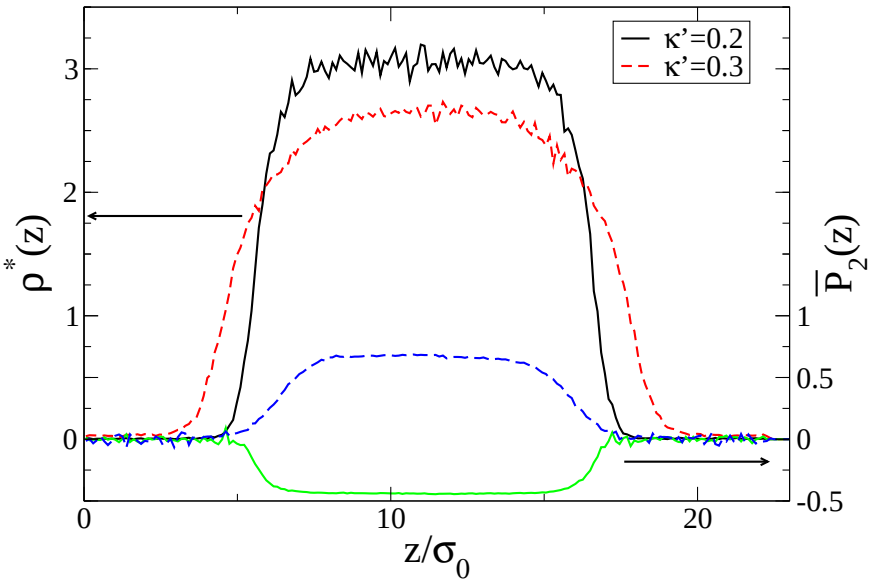

Figure 4. Density ρ^* (upper curves) and orientational order $\overline{P}_2(z)$ (lower curves) profiles at $T^* = 2.20$ for Gay-Berne fluids with $\kappa = 0.3$ and $\kappa' = 0.2$ (continuous lines) and $\kappa' = 0.3$ (dashed lines).

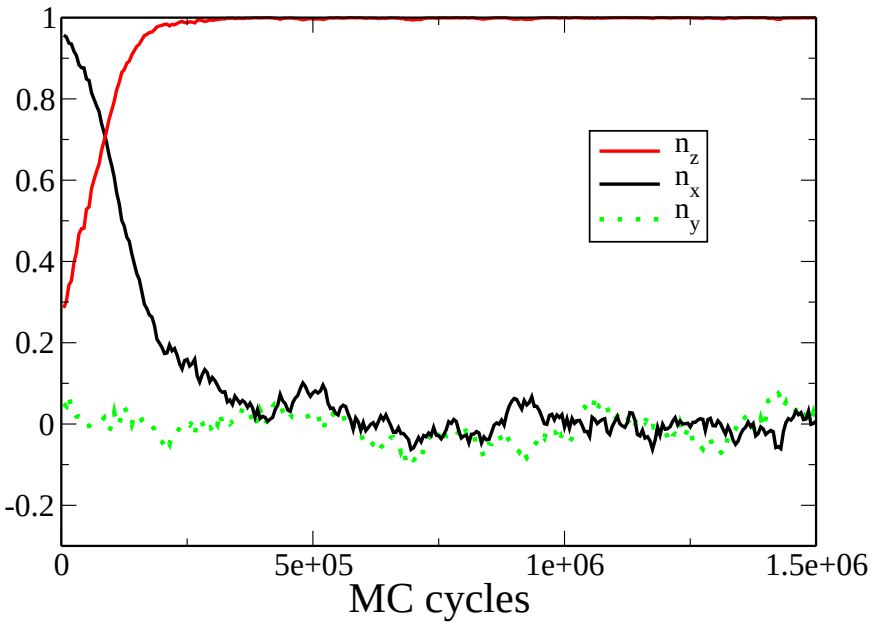

Figure 5. Evolution of the nematic director components for a Gay-Berne fluid with $\kappa = 0.3$ and $\kappa' = 1$ for $T^* = 1.1$ in presence of a nematic-vapour interface, starting at a planar configuration.

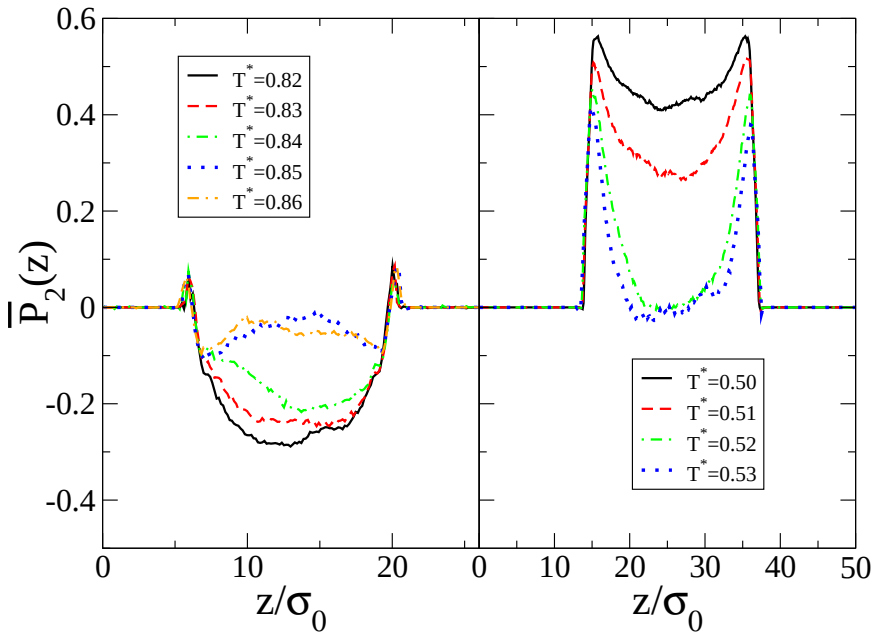

Figure 6. Left panel: plot of the orientational order profile for $\kappa = 0.5$, $\kappa' = 0.3$, $N = 4000$ and $T^* = 0.82$ (continuous line), 0.83 (dashed line), 0.84 (dot-dashed line), 0.85 (dotted line) and 0.86 (dot-double dashed line). The nematic-isotropic-vapour triple point temperature is $T^* = 0.845 \pm 0.005$. Right panel: plot of the orientational order profile for $\kappa = 0.5$, $\kappa' = 1.0$, $N = 4116$ and $T^* = 0.50$ (continuous line), 0.51 (dashed line), 0.52 (dot-dashed line) and 0.53 (dotted line). The nematic-isotropic-vapour triple point temperature is $T^* = 0.505 \pm 0.005$.

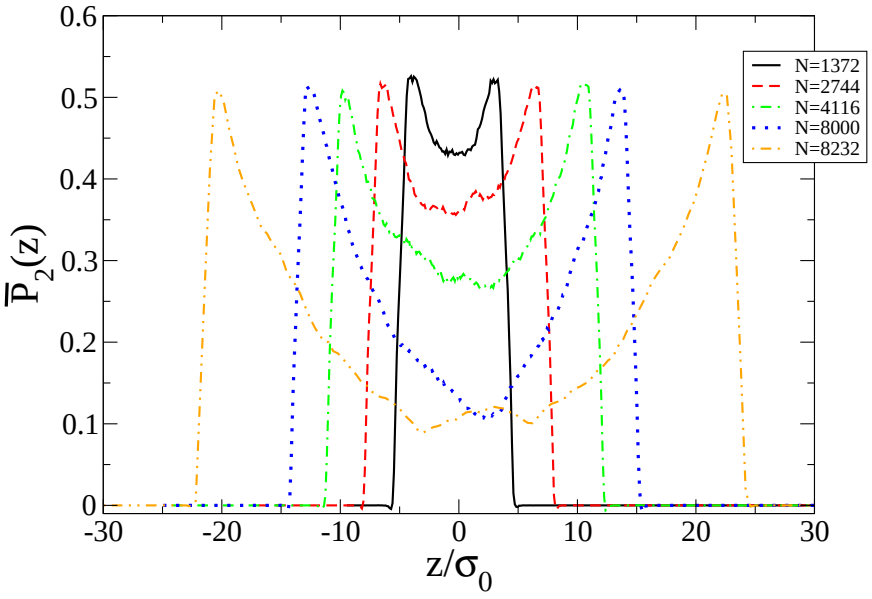

Figure 7. Dependence on the number of particles N of the simulated orientational order profile for $\kappa = 0.5$, $\kappa' = 1.0$ and $T^* = 0.51$: $N = 1372$ (continuous line), 2744 (dashed line), 4116 (dot-dashed line), 8000 (dotted line) and 8232 (double dot-dashed line).

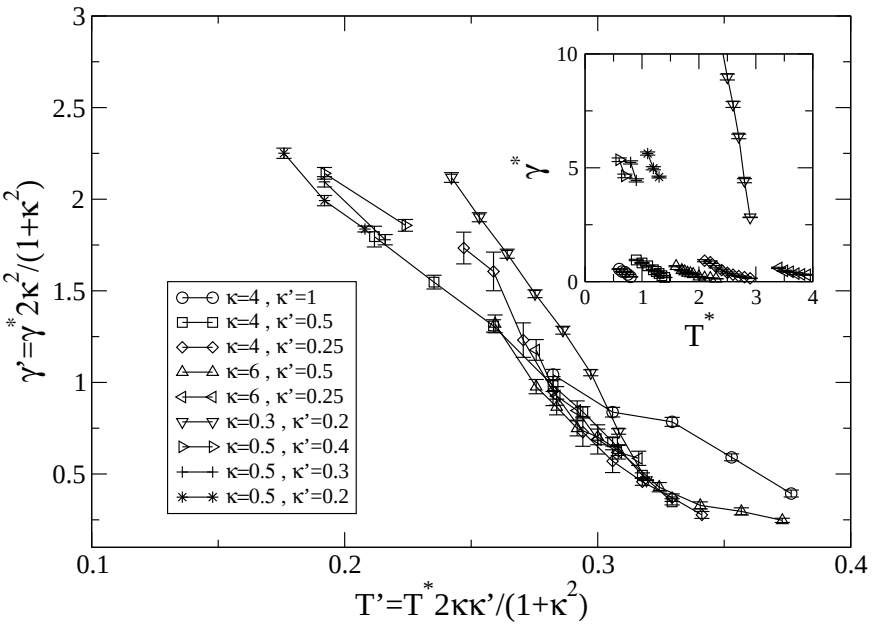

Figure 8. Plot of the rescaled nematic-vapour surface tension $\gamma' = 2\kappa^2\gamma^*/(1+\kappa^2)$ as a function of the rescaled temperature $T' = 2\kappa\kappa' T^*/(1+\kappa^2)$ for planar anchoring: $\kappa = 4$, $\kappa' = 1$ (circles); $\kappa = 4$, $\kappa' = 0.5$ (squares); $\kappa = 4$, $\kappa' = 0.25$ (diamonds); $\kappa = 6$, $\kappa' = 0.5$ (triangles up); $\kappa = 6$, $\kappa' = 0.25$ (triangles left); $\kappa = 0.3$, $\kappa' = 0.2$ (triangles down); $\kappa = 0.5$, $\kappa' = 0.4$ (triangles right); $\kappa = 0.5$, $\kappa' = 0.3$ (pluses) and $\kappa = 0.5$, $\kappa' = 0.2$ (stars). Inset: Plot of the reduced γ^* vs T^*. The meaning of the symbols is the same as in the main plot.

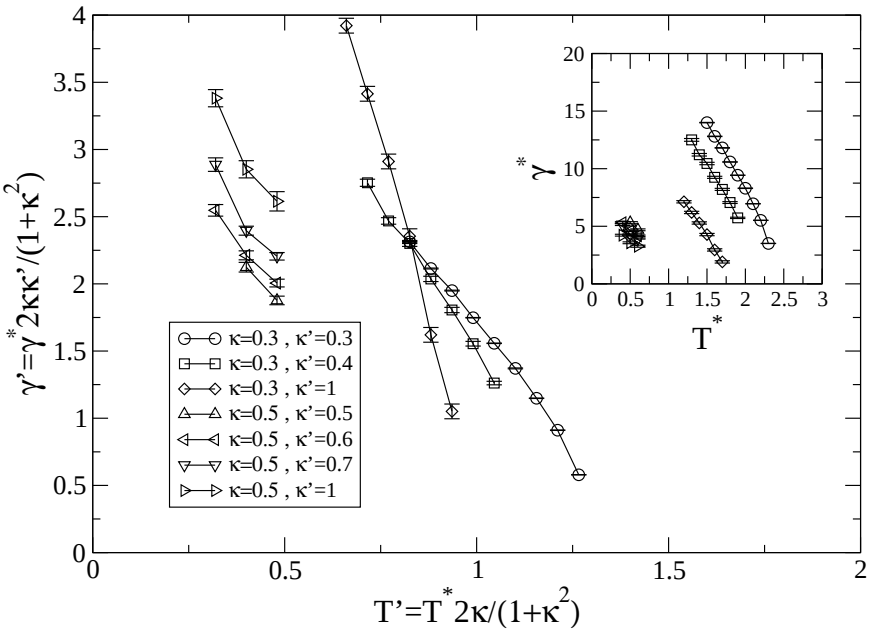

Figure 9. Plot of the rescaled nematic-vapour surface tension $\gamma' = 2\kappa\kappa'\gamma^*/(1+\kappa^2)$ as a function of the rescaled temperature $T' = 2\kappa T^*/(1+\kappa^2)$ for homeotropic anchoring: $\kappa = 0.3$, $\kappa' = 0.3$ (circles); $\kappa = 0.3$, $\kappa' = 0.4$ (squares); $\kappa = 0.3$, $\kappa' = 1$ (diamonds); $\kappa = 0.5$, $\kappa' = 0.5$ (triangles up); $\kappa = 0.5$, $\kappa' = 0.6$ (triangles left); $\kappa = 0.5$, $\kappa' = 0.7$ (triangles down) and $\kappa = 0.5$, $\kappa' = 1$ (triangles right). Inset: Plot of the reduced γ^* vs T^*. The meaning of the symbols is the same as in the main plot.